Published in final edited form as:
Appl Magn Reson. 2009 ; 35(2): 285–318. doi:10.1007/s00723-008-0162-0.

Coupling of Waveguide and Resonator by Inductive and Capacitive Irises for EPR Spectroscopy

R.R. Mett[1,2], **J.W. Sidabras**[1], and **J.S. Hyde**[1]

1*Department of Biophysics, Medical College of Wisconsin, Milwaukee, Wisconsin, USA*

2*Milwaukee School of Engineering, Milwaukee, Wisconsin, USA*

Abstract

An analytic circuit model for slot coupling from a waveguide to a loop-gap resonator (LGR) in a context of electron paramagnetic resonance (EPR) spectroscopy is presented. The physical dimensions of the waveguide, iris, LGR, and aqueous sample are transformed into circuit values of inductance, capacitance, and resistance. These values are used in a solution of circuit equations that results in a prediction of the rf currents, magnitude and phase, frequency, and magnetic and electric stored energies near critical coupling. The circuit geometry reflects magnetic flux conservation between the iris and LGR as well as modification of the outer loop LGR currents by the iris. Unlike conventional models, coupling is not explicitly based on a mutual inductance between the iris and LGR. Instead, the conducting wall high frequency rf boundary condition is used to define surface currents, regions, and circuit topology with lumped-circuit values of self-inductance, capacitance, and resistance. Match is produced by a combination of self-inductive and capacitive circuit coupling. Two conditions must be met to achieve match. First, the equivalent resistance of the LGR as seen by the iris must be transformed into the waveguide characteristic impedance. This transformation is met at a particular frequency relative to the natural LGR resonance frequency. The frequency shift magnitude is largely determined by the LGR properties, weakly dependent on iris length and placement, and independent of other iris dimensions. The second condition for match is that the iris reactance at this frequency shift must cancel the residual reactance of the LGR. This second condition is sensitive to the iris dimensions. If both conditions are not simultaneously satisfied, overcoupling or undercoupling results. A slotted iris of equal length to the size of the large dimension of the waveguide is found to have many properties opposite to a conventional iris of shorter length. Notably, the magnetic field near the iris tends to reinforce rather than oppose the magnetic field in the resonator. The long iris improves the LGR EPR performance by providing increased rf magnetic field homogeneity at the sample, higher signal, and reduced total frequency shift since the shifts due to sample and iris tend to cancel. Investigations reveal that the first match condition can be adjusted by LGR dimensional changes and such adjustment can eliminate the frequency shift. Results are consistent with Ansoft High Frequency Structure Simulator (Version 10.1, Ansoft Corporation, Pittsburgh, PA) simulations and can be extended to cavity resonators.

Keywords

iris; EPR; loop-gap resonator

Author to whom correspondence should be addressed: James S. Hyde Department of Biophysics Medical College of Wisconsin 8701 Watertown Plank Road Milwaukee, WI 53226-0509 Phone: (414) 456-4005 Fax: (414) 456-6512 E-mail: E-mail: jshyde@mcw.edu.

1 Introduction

Mett and Hyde [1] have studied the influence of round and slotted irises on microwave leakage from magnetic field modulation slots cut perpendicular to the axis of TE_{011} cavities at Q-band. They found that a thin slotted iris has significantly less leakage than a round iris because the slotted iris makes a smaller perturbation on the TE_{011} mode than the round iris. A similar observation was made using the finite element computer program Ansoft High Frequency Structure Simulator (HFSS) (Version 10.1, Ansoft Corporation, Pittsburgh, PA) in loop-gap resonators (LGRs) of significant length. The authors were surprised at the level of mode perturbation, even at the sample, caused by round and slotted irises in a 10-mm-long 3-loop-2-gap resonator at Q-band (Fig. 1), despite the expected shielding effects of the gaps. The ratio of this LGR length to free space wavelength is 114% and other dimensions are given in Table 1. Radio frequency magnetic field energy density uniformity was diminished by 8-15% compared to eigenmode by these couplers, Fig. 2(a). Uniform magnetic field at the sample is required to achieve uniform spin saturation. In an attempt to lower the level of mode perturbation caused by the iris, narrower and longer irises were tried. It was found possible to extend the iris length across the full WR-28 waveguide width as shown in Fig. 1 with iris dimensions given in Table 2. This long iris was observed to have many properties opposite or dual to those of a conventional slotted iris of length less than half the long waveguide dimension and those of a round iris. These properties include the phases of the rf fields and currents in the resonator relative to those near the iris, the stored energy type in the iris, the frequency at match relative to the resonator natural resonance frequency (frequency shift), and the sign of the iris reactance (inductive vs. capacitive). In addition, the rf magnetic energy density uniformity at the sample was improved by the long iris compared to the eigenmode solution, Fig. 2(a). This paper presents an analysis and circuit model of iris coupling of a waveguide to an LGR. Although the analysis is done specifically for an LGR, treatment of a cavity resonator follows with little modification. The model was developed in close conjunction with Ansoft HFSS.

The LGR was introduced for use in EPR spectroscopy in the simplest possible cross-sectional geometry, Fig. 3(a), [2] and later extended to numerous other cross-sections including those shown in Figs. 3(b)-(d). The literature has been reviewed by Hyde and Froncisz [3] and by Rinard and Eaton [4]. Iris coupling between a waveguide and a 3-loop-2-gap LGR of 1-mm length has been done at Q-band, but there is no rationale given for the design [5, 6].

Iris coupling between waveguide and cavity is typically modeled by a mutual inductance *M* between the iris and the cavity inductance [1,7-9]. After extensive investigation using Ansoft HFSS, models with mutual inductance were found to be inadequate to explain the iris coupling behavior between waveguide and 3-loop-2-gap LGR for irises of different sizes at Q-band. A simple mutual inductance model following ref. 1 was found to mimic some of the observations, including phases of rf currents and the input impedance, but not others such as frequency shift. The addition of the distributed nature of the iris into the model, Sect. 2.2, including mutual inductance between iris and LGR outer loop, was found to increase disparities between the model and HFSS observations, and a rationale for choosing the sign and value of *M* remained unsatisfactory.

In the present work, the metallic wall high frequency rf boundary condition, which relates surface current to magnetic field [8], was used to define surface currents, distinct regions, and circuit topology of the coupled iris-LGR with lumped-circuit values of capacitance, resistance, and self-inductance with no mutual inductance. That it is possible to obtain a complete circuit model of the coupled iris-LGR without mutual inductance is perhaps surprising. However, we show in Appendix A that the equivalent self-inductance of a coil in the presence of a metallic rf shield is equivalently expressible in terms of mutual inductance or self-inductance. The effect

of the mutual inductance of the shield on the coil in the high frequency rf limit is to induce an rf current on the outside surface of the coil. The separation of the total current on the coil into an inner current and an outer current leads to the ability to treat the coil as two self-inductances in parallel with no mutual inductance between them. The mutual and self inductance models differ in the definition of the coil currents. The results are consistent with a statement by Grover [10]: “Self-inductance is merely a special case of mutual inductance.”

In the present work, the circuit model geometry reflects flux conservation between iris and LGR, includes capacitive and inductive circuit coupling, and accounts for the influence of the iris on the LGR outer loop currents. In this model, the geometrical dimensions of the LGR, iris, and waveguide are used to calculate circuit values of self-inductance, capacitance, and resistance, including the effects of sample. These circuit values then determine the solution to the circuit equations and predict the input impedance, rf currents, frequency shift, and magnetic and electric stored energies. The circuit is a pi network with the bridge element an inductance formed by the part of the LGR outer loop cut by the iris. The circuit can be cast into an equivalent form having an *effective* mutual coupling between two resonant circuits described by Terman [9]. The effective mutual coupling represents combined capacitive and self-inductive (complex) coupling between primary (waveguide/iris) and secondary (LGR), although with no mutual inductance.

Two conditions must be met to achieve critical coupling (match). First, the equivalent resistance of the LGR as seen by the iris must be transformed into the waveguide characteristic impedance. Due to the behavior of the LGR resistance with frequency, this transformation typically occurs at a particular frequency relative to the natural LGR resonance frequency. This frequency shift magnitude is strongly dependent on the LGR and sample dimensions, weakly dependent on the iris length and placement, and independent of other iris dimensions. The second condition for match is that the iris reactance at this frequency shift must cancel the residual reactance of the LGR. This second condition is sensitive to the iris dimensions. If both conditions are not simultaneously satisfied, overcoupling or undercoupling results. The first match condition completely determines the frequency shift magnitude, and so LGR and iris design can reduce or eliminate this frequency shift, or tailor it for example to the needs of the EPR spectroscopist, who prefers no difference between the frequencies at match with and without sample.

2 Theory

A mechanical drawing of the 3-loop-2-gap 10-mm-long Q-band LGR introduced by Mett, Sidabras, and Hyde [11] with iris coupling to a WR-28 waveguide is shown in Fig. 1. The LGR and sample dimensions are shown in Table 1. The lumped circuit model that reflects the interaction between LGR, iris, and waveguide is developed in stages below. For simplicity, we assume that the symmetry planes of the waveguide, iris, and LGR coincide so that two half-circuits in parallel describe the whole. With further analysis, this symmetry can be removed. At points in the development of the theory, predictions of the circuit model calculated with Mathematica (Version 6, Wolfram Research, Inc., Champaign, IL) were compared with Ansoft HFSS simulations. A Dell Precision 690 workstation with dual dual-core 3.0 GHz processors and 16 GB of RAM with Windows XP 64-bit was used to run the program. Both eigenmode and driven solution methods were used.

2.1 Circuit Model of LGR

Since the iris intercepts one of the outer loops of the LGR (Fig. 1), we take as a first approximation the LGR circuit seen by the iris, Fig. 4. Accordingly, the LGR input impedance is given by Eq. (1) assuming $e^{j\omega t}$ time dependence:

$$Z_{LGR}=R_o+j\omega L_o+\frac{1}{j\omega C'+\frac{1}{R_i+j\omega L_i+\frac{1}{j\omega C'+\frac{1}{R_o+j\omega L_o}}}}. \quad (1)$$

The lumped circuit values of self-inductance, capacitance, and resistance are expressed in terms of the LGR dimensions and conductivity as shown in Appendix B. The derivation follows from Mett et al. [11] and corresponds to the LGR at cutoff. At cutoff, the rf currents are perpendicular to the LGR axis and the rf fields are axially uniform (except within one radius of the LGR ends). Reference [11] also shows how an rf impedance at the ends of the LGR causes a shift in the resonance frequency from cutoff and a corresponding rf field axial non-uniformity. That axial full-wave analysis is shown to account for a majority of resonance frequency deviation from cutoff and field non-uniformity. The LGR ends can be designed to have an infinite rf impedance and the LGR then resonates with uniform fields at cutoff. Since the present work is about the influence of a coupling iris on the LGR, for simplicity we do not include the axial full-wave analysis, although such effects could be included with further analysis. The frequency shifts due to coupling predicted by the circuit model are relative to cutoff. These are compared to the frequency shifts predicted by finite element modeling of driven mode with the iris relative to eigenmode without.

Near resonance, the magnetic flux in the inner LGR loop is shared between the outer loops. This conservation of flux can be combined with the expression for the peak magnetic energy of the system to derive the equivalent inductance,

$$L_{eq}=mL_o\left(1+m\frac{L_o}{L_i}\right), \quad (2)$$

and with the expression for the dissipated power to obtain the equivalent resistance,

$$R_{eq}=m\left(R_o+m\left(\frac{L_o}{L_i}\right)^2 R_i\right), \quad (3)$$

looking into the outer loop, Fig. 4. These equations were written for m gaps and m outer loops; although in Fig. 4, $m = 2$. It can be shown that Eq. (3) reduces to Eq. (2) with the replacement $R \rightarrow L$. These equations, which can also be derived from Eq. (1), reflect how flux conservation in the LGR magnifies the resistance of the inner loop as seen from the outside. The effect is transformer-like, although in the circuit model there is no mutual inductance. The quality factor is given by

$$Q=\frac{\omega_0 L_{eq}}{R_{eq}}, \quad (4)$$

where the subscript zero indicates the natural LGR resonance frequency. As shown in Appendix B, the LGR loop resistances are caused by the rf current flow on the inner surface of the conducting loop and part of the gap. Equations (2)-(4) and the equations of Appendix B give Q values within 1.5% of those of the LGR at cutoff predicted by Ansoft HFSS. When a sample is inserted to the LGR inner loop, the circuit is loaded by an effective sample resistance added to the inner loop resistance of Eq. (B9), $R_i \rightarrow R_i + R_s$. The value of R_s is calculated from Eqs. (2)-(4) using a sample-loaded LGR Q value that can be obtained either by experimental

measurement or by finite element modeling. With such a sample resistance, it is found that the dependence of impedance with frequency predicted by Eq. (1) near resonance is fully consistent with the behavior of the coupled LGR reflection coefficient with frequency predicted by driven mode Ansoft HFSS.

We can also write the equivalent capacitance as

$$C_{eq}=\frac{C\prime}{m\left(1+m\frac{L_o}{L_i}\right)^2}, \tag{5}$$

and so the (natural) LGR resonance frequency

$$f_0=\frac{1}{2\pi\sqrt{L_{eq}C_{eq}}}. \tag{6}$$

With the lumped circuit values of Appendix B, this frequency is the LGR cutoff frequency. Equations (2), (5), and (6) give identical results to Eqs. (2)-(7) of ref. 11. (The effect of Q on the resonance frequency is less than four parts per million at a Q of 200.)

The LGR equivalent circuit (Fig. 4) is a parallel *R-L-C* circuit driven by a series *R-L* and has properties of both parallel and series *R-L-C* circuits. As is well known, the resistance of a parallel *R-L-C* circuit as a function of frequency has a Lorentzian shape peaked at its natural resonance frequency. Similarly, the admittance of a series *R-L-C* circuit has a Lorentzian shape peaked at the natural resonance frequency. The corresponding reactance and susceptance of these respective circuits have the shape of a Lorentzian derivative. For the LGR, the conductance as a function of frequency has a Lorentzian shape peaked at the natural resonance frequency f_0, Eq. (6), where it is equal to $1/R_{eq}$. The susceptance has the shape of a Lorentzian derivative with an offset value of approximately $-(\omega L_o)^{-1}$ at the natural resonance frequency since the LGR circuit is broken at the outer loop. These can be summarized by

$$\frac{1}{Z_{LGR}\ (f_0)} \cong \frac{1}{R_{eq}}+\frac{1}{j\omega L_o}, \tag{7}$$

and follow from Eq. (1) in the limits $R_{eq}R_i \ll (\omega L_i)^2$ and $R_o \ll R_{eq}$. The width of the Lorentzian at half maximum is $\Delta f_w = f_0/Q$. The variation of the LGR admittance near f_0 determines the frequency of critical coupling, as discussed further in Sect. 2.5 and the results section. The real and imaginary parts of the LGR impedance also have Lorentzian and Lorentzian-derivative shapes, respectively, but the Lorentzian center frequency is displaced several percent below both f_0 and the frequency of critical coupling.

2.2 Circuit Model of Iris

A drawing of the rf currents flowing around the iris is shown in Fig. 5(a) and can be compared to the mechanical drawing of Fig. 1. The iris has a capacitance largely across its center and a self-inductance largely on each end. A naive approach suggests that we might assign a capacitance to the center half,

[2]Since the resistances are neglected in the calculation, the accuracy of this predicted match frequency decreases as f_m approaches the range of frequencies approaches the range of frequencies within the Lorentzian half width $f_0 \pm f_0/Q$.

$$C=\frac{\varepsilon_0 l_c t_c}{4w_c}, \tag{8}$$

and a self-inductance to the outer half,

$$L=\frac{\mu_0 w_c l_c}{4t_c}, \tag{9}$$

of the half-iris, where l_c, w_c, and t_c are the total length, width, and wall thickness of the coupling iris, respectively; ε_0 is the electric permittivity of free space; and μ_0 is the magnetic permeability of free space. Equations (8) and (9) can be refined by considering that iris current flows oppose one another across the iris thickness, and that the current flow is directed primarily along the iris length dimension, Fig. 5(a). Therefore, the iris can be viewed as two parallel conducting strips shorted at each end. The configuration is a two-conductor transmission line supporting an electromagnetic mode transverse to the iris length (TEM). It is well known that the electromagnetic solutions for a TEM mode consist of the electrostatic solution with the magnetic solution derivable from the electrostatic field [8], [12]. Consequently, we can use an analytic electrostatic solution for the capacitance per unit length of two long parallel conducting strips given by Smythe [13] and that has been applied to the LGR gap in Appendix B and ref. 11. The solution takes the form of a factor γ that multiplies the capacitance per unit length $\varepsilon_0 t_c/w_c$, and thus the quarter-iris length given by Eq. (8),

$$C_c=\gamma C. \tag{10}$$

This factor is a function of the ratio t_c/w_c through elliptic integrals. Due to dimensional definitions, we replace the ratio w/t in Eqs. (B6) and (B7) of Appendix B by t_c/w_c. In practice, a different stray capacitance correction using Eq. (16) of ref. 11 produces similar results. These corrections cannot be used simultaneously because the capacitance is overestimated.

Because of the TEM transmission line mode, the product of the capacitance per unit length and the inductance per unit length along the iris length dimension is $\varepsilon_0\mu_0$ [8], [12]. Therefore, the iris inductance of a quarter iris length, Eq. (9), must also be corrected by the same factor,

$$L_c=L/\gamma. \tag{11}$$

The $C_c L_c$ product then remains a function only of the iris dimension of length. A further correction to Eqs. (10) and (11) can be made by further considering the iris as a transmission line. As shown by Jackson [12] and in the LGR gap discussion of Appendix B, a capacitor formed by two parallel metallic strips of dimensions $l_c/4$ and t_c a distance w_c apart and fed along the length has a capacitance given by Eq. (8) with a series inductance equal to one-third of Eq. (9). Similarly, if these strips are shorted, we obtain an inductance given by Eq. (9) with a parallel capacitance equal to one-third of Eq. (8). Since the iris is symmetric about its center, where there is also a current null, the center capacitance is fed from the end inductance. These results can be combined into the lumped circuit model of the isolated half-iris shown in Fig. 5 (b), where

$$L_{cc}=L_c/3, \tag{12}$$

$$C_{cc}=C_c / 3. \tag{13}$$

The total input impedance

$$Z_{in}=\frac{v_{in}}{2i_{in}} \tag{14}$$

of the isolated iris is therefore

$$Z_{iris}=\frac{1}{2j\omega C_c+\frac{2}{j\omega L_{cc}+\frac{1}{j\omega C_{cc}+\frac{1}{j\omega L_c}}}}. \tag{15}$$

The same model can be obtained from the impedance of a length $l_c/4$ of open transmission line, $-jZ_0\cot(kl_c/4)$, and shorted transmission line, $jZ_0/\cot kl_c/4$, where the characteristic impedance $Z_0=\sqrt{\left(\frac{\mu_0 w_c}{l_c\gamma}\right)/\left(\frac{\varepsilon_0 l_c\gamma}{w_c}\right)}$ and the wavenumber $k=\omega/c$, using the first two terms in the expansion $\cot x = 1/x - x/3 - \ldots$, which converges for $0<|x|<\pi$. Iris resistances can be included but are typically negligible because of the low primary Q as discussed in Sect. 2.6. An exception is the unusual case of a strongly resonant iris discussed in Sect. 3.2. The distributed nature of the iris is largely captured by this model. Analysis of Eq. (15) shows that the self-resonance frequency of the isolated iris is given by

$$f_c=\frac{\sqrt{\frac{3}{2}\left(5-\sqrt{21}\right)}}{2\pi\sqrt{C_c L_c}}, \tag{16}$$

which is about 79.1% ($\cong\pi/4$) of the resonance frequency of C_c and L_c alone. The frequency predicted by Eq. (16) is within 3% of the self-resonance frequency determined by Ansoft HFSS eigenmode simulation for an isolated iris. Furthermore, Eq. (16) with (8)-(11) is consistent with the expression for the resonance frequency of a shorted two-conductor TEM transmission line of length l_c, $f_c=\frac{c}{2l_c}$ to within 1%. It is possible to use exact transmission line impedances, which can be a subject of future investigation.

An alternative approach to finding the iris impedance is to use the theory of obstacles and windows in waveguides [14]. Because the iris wall thickness t_c is comparable to the iris opening width w_c, the iris is considered an obstacle of finite thickness. The special case of iris length equal to the large waveguide dimension is treated explicitly as a capacitive obstacle of large thickness in Sect. 8-8 of ref. 14. For typical dimensions that provide match to the LGR discussed below, the nonlimited form gives an iris capacitive reactance magnitude 14% lower (more capacitive) than Eq. (15). The discrepancy is likely because the waveguide method treats only the first two waveguide modes and because the method assumes that there is waveguide present on both sides of the iris. Instead, the presence of the LGR outer loop must be accounted for to predict the full behavior of the iris. This is the subject of the next section.

2.3 Iris Connection to LGR Outer Loop

By the geometry of Fig. 1, all the magnetic flux penetrating the top end of the iris must enter the LGR loop, go through the central part of the LGR outer loop, and leave the LGR loop by penetrating the bottom end of the iris. Due to the metallic wall high frequency rf boundary

condition, which relates surface current to magnetic field [8], there can be no magnetic flux going through one end of the iris without a corresponding current i_c flowing around the iris end, Fig. 5(b). By definition, the ratio of this magnetic flux to the current i_c is L_c. Similarly, by the metallic boundary condition on the LGR outer loop, there can be no magnetic flux penetrating the outer loop without a corresponding current in the LGR outer wall, and the ratio of this flux to the current is the inductance of this part of the outer loop. This geometry is reflected in the circuit of Fig. 5(c), which shows the half-circuit of the iris coupled to the part of the LGR outer loop that extends from one end of the iris to the other. Here, the inductance of the part of the outer loop that the iris couples to is given by

$$L_e = sL_o \frac{4l}{l_c}, \tag{17}$$

which is the total inductance of the outer loop L_o scaled by $l_c/4$ and then multiplied by an order unity geometrical scale factor s, which quantifies the extent that the iris flux occupies the LGR outer loop. We chose to scale the inductance by a basis of $l_c/4$ (instead of $l_c/2$) because of how the distributed currents from the LGR outer loop flow around the iris, the mapping of these currents to i_o'', and the connection to the iris center (see Figs. 5(a) and 6). However, the choice of basis is arbitrary because scaling is ultimately determined by the value of the parameter s. The determination of the value of s is further discussed in the Results section. Because of the inverse scaling of the outer loop inductance to length l, Eq. (B4), s^{-1} can also be viewed as a length multiplier of L_e over its basis length $l_c/4$. It is possible to write the condition for magnetic flux conservation between the iris and L_e

$$\Phi_c + \Phi_{cc} = \Phi_e$$

as

$$L_c i_c + L_{cc} i_{cc} = L_e i_o''$$

which, by Faraday's Law, when multiplied by $j\omega$ becomes a statement of Kirchhoff's Voltage Law (KVL) as required by the circuit of Fig. 5(c). Flux conservation is thus a consequence of the circuit geometry: the total flux from half the iris goes through the part of the LGR outer loop defined by L_e. Thus, KVL implies that any two self-inductances in parallel have the same magnetic flux, but this does not necessarily mean that the return flux from one goes into the other, nor does this imply that there is a mutual inductance between them. Appendix A includes a discussion of the relationship between mutual and self-inductances and rf current definitions for the case of a shielded coil. In the present case, due to the rf current definitions and the metallic wall boundary conditions, the magnetic flux from the iris self-inductances go into part of the LGR outer loop. There is no mutual inductance between the iris and LGR outer loop because each of the inductors is embedded in a metallic wall or block, which forces any flux penetrating the inductor to be caused by a current flowing in the metallic surface that forms the inductor.

The coupling of the iris flux to part of the LGR outer loop is indicated by the parallel arrangement of L_e across the iris shown in Fig. 5(c) and alters the self-resonance frequency of the iris. For the long iris of dimensions given in Table 2 (length 7.62 mm), the circuit of Fig. 5(c) predicts that the iris self-resonance frequency is raised from 19.8 GHz in isolation to 25.1 GHz when coupled to the LGR outer loop of dimensions of Table 1 (outer loop radius 1.029 mm), with the flux occupation factor $s = 1$. This is within 0.25% of the frequency predicted by

Ansoft HFSS eigenmode simulations with shorted gap. Significantly shorter irises have significantly higher self-resonance frequencies, which can be influenced by coupling to higher order modes that are not accounted for in the model.

2.4 Circuit Model of Connected Iris and LGR

We build on the results of the previous three sections and construct the half-circuit model of the combined iris and LGR, Fig. 6. Here, we separate the total LGR outer loop half-circuit inductance $2L_o$ into two parts,

$$2L_o=\frac{1}{\frac{1}{L_e}+\frac{1}{L'_e}}, \tag{18}$$

so that their parallel combination gives the inductance of the half outer loop. Equation (18) defines L'_e. Similarly, since the outer loop resistance is caused by the same surface current that produces the inductance (see Eq. (B8) discussion), we modify an outer loop resistance,

$$R_e=sR_o\frac{4l}{l_c}, \tag{19}$$

and break it into two parts to define R'_e,

$$2R_o=\frac{1}{\frac{1}{R_e}+\frac{1}{R'_e}}. \tag{20}$$

The resistance is a small correction to the total outer loop impedance. By the arguments of the previous section, the circuit connections of Fig. 6 with KVL imply (neglecting R_o) the magnetic flux conservation rule

$$\Phi_c+\Phi_{cc}=\Phi_e+\Phi'_e,$$

or

$$L_c i_c+L_{cc} i_{cc}=L_e i''_o+L'_e\left(i''_o-i_o\right). \tag{21}$$

In the absence of iris flux, these equations show that the flux in L_e and L'_e is the same (the sign is due to the current direction definition), and this flux can also be shown to be equal to the flux in $2L_o$ (and L_o). Since Eq. (21) is implied by the circuit equations, it can be substituted for any one of the circuit relations implied by Fig. 6 without changing the solution.

The circuit of Fig. 6 shows that the voltage developed across the iris drives part of the LGR outer loop inductance L_e, which in turn drives the modified LGR impedance Z'_{LGR}. The inductance L_e acts as the bridge element in a pi network between the impedances Z_{iris} and Z'_{LGR}. The size of L_e influences the coupling strength, and its value depends on the length of the iris. The shape of the iris determines not only the iris impedance but also the value of L_e, which in turn influences the modified LGR impedance Z'_{LGR}. This complex interaction between the iris and the LGR is captured by the circuit of Fig. 6.

It can be shown that the admittance of the series combination of L_e and Z'_{LGR} is a simple transformation of the LGR admittance from Eq. (1),

$$\frac{1}{Z'_{LGR}+(j\omega L_e+R_e)/2}=\left(\frac{2L_o}{L_e}\right)^2\left[G_{LGR}+jB_{LGR}-\frac{1}{j\omega L_o+R_o}\right]+\frac{2}{j\omega L_e+R_e}, \tag{22}$$

where $Y_{LGR}= 1/Z_{LGR}=G_{LGR}+jB_{LGR}$. As shown by the circuit of Fig. 6, the admittance given by Eq. (22) is in parallel with the iris. Since L_e is always greater than or equal to $2L_o$, this transformation shows that the LGR conductance is reduced by the parallel combination of L_e and L'_e. The same is true for the susceptance but for the inductive offsets (see Eq. (7)). The term in square brackets is real at the natural LGR resonance frequency.

2.5 Conditions for Match

Due to symmetry, the voltage and current at the input to the iris is the same voltage and current at the end of the waveguide. Thus, match is obtained when the input impedance determined by this voltage to current ratio is near the characteristic impedance of the waveguide Z_0. The complete system of equations describing match according to the half-circuit of Fig. 6 is given in Appendix C. This system is solved for the total input impedance Eq. (14) and also rf current ratios between any two chosen currents. The input impedance and current ratios are examined as functions of frequency and Q near match with dimensions for various irises and LGRs in order to observe their behavior near match and to compare them to Ansoft HFSS simulations.

Insight into the system is obtained by setting the input impedance equal to the characteristic impedance of the waveguide, Eq. (A4). From Eq. (22), we obtain

$$Y_0=\left(\frac{2L_o}{L_e}\right)^2 G_{LGR}, \tag{23}$$

$$B_{iris}=\frac{2}{\omega L_e}-\left(\frac{2L_o}{L_e}\right)^2\left[B_{LGR}+\frac{1}{\omega L_o}\right], \tag{24}$$

where $Y_0=1/Z_0$,$B_{iris}=j/Z_{iris}$, and we have assumed $R_o^2 \ll (\Omega L_o)^2$ and $R_e^2 \ll (\Omega L_e)^2$. Equations (23) and (24) are the two conditions needed for critical coupling. Because $G_{LGR}(f)$ has the form of a Lorentzian peaked at the natural LGR resonance frequency f_0, Eq. (23) is typically satisfied only at two particular frequencies, $f_0 \pm \Delta f$. The iris length has an influence on the ratio $2L_o/L_e$, but the other iris dimensions do not. Therefore, Eq. (23) can only be satisfied through a shift in frequency Δf relative to the natural LGR resonant frequency. It represents the required transformation to take the LGR conductance to the waveguide characteristic admittance for critical coupling. Iris dimensions have little influence on Δf. Typically, Δf is many times the Lorentzian half-width Δf_w. Once Eq. (23) is met, the iris susceptance must also be adjusted to satisfy Eq. (24). Since $B_{LGR}(f)$ has the form of a Lorentzian derivative with appropriate offsets, the iris will only meet this condition at a frequency Δf above or below f_0, depending on whether the iris is capacitive or inductive, respectively. We define the match frequency f_m to be the frequency where the conditions of Eqs. (23) and (24) are both met. If both conditions are not simultaneously satisfied, overcoupling or undercoupling results.

The equivalent conditions for match expressed in terms of the impedances are given in Appendix D. The impedance system cannot be described in a simple or intuitive way because

the LGR impedance does not have symmetry about f_0 and because the impedance transformation between Z_{LGR} and Z'_{LGR} is more complicated than the transformation in Eq. (22). The impedance system is further discussed in the following section and Appendix D.

2.6 Connection to Generalized Coupled Circuit Theory

The combined iris-LGR circuit of Fig. 6 can be described in terms of the equivalent coupled circuit of Fig. 7, which is a generalization of two (mutual) inductively coupled circuits [9]. The circuits are coupled through an effective mutual inductance M_{eff}, which is a result of the combined capacitive and direct self-inductive coupling (with no mutual inductance) reflected in the circuit of Fig. 6.[1] The primary impedance is the impedance looking into the primary with open secondary, which, from Fig. 6, corresponds to the condition $Z'_{LGR} \to \infty$,

$$Z_P = Z_{iris},$$

where Z_{iris} is given by Eq. (15). The secondary impedance is the impedance looking into the secondary with open primary, which corresponds to the condition that the waveguide characteristic impedance $Z_0 \to \infty$,

$$Z_s = Z_{iris} + (j\omega L_e + R_e)/2.$$

The iris appears in both the primary and secondary equivalent circuits. The coupling strength between the primary and secondary depends on the impedance of the primary with shorted secondary, which is found from setting $Z'_{LGR} \to 0$,

$$Z_{Ps} = \frac{1}{\frac{1}{2Z_{iris}} + \frac{1}{j\omega L_e + R_e}},$$

and so the coupling constant

$$k_c = \sqrt{1 - \frac{Z_{Ps}}{Z_P}} = \frac{1}{\sqrt{1 + \frac{j\omega L_e + R_e}{2Z_{iris}}}} \cong \frac{1}{\sqrt{1 + \frac{\omega L_e}{2X_{iris}}}},$$

where $jX_{iris} = Z_{iris}$. The effective mutual coupling then reduces to the perhaps surprisingly simple expression

$$M_{eff} = k_c \sqrt{\frac{Z_P Z_S}{(j\omega)^2}} = \frac{X_{iris}}{\omega}. \tag{25}$$

Several conclusions can be drawn from these results. When the resonance frequency of the iris is higher than the frequency of the LGR, Z_{iris} is inductive. This is true for the conventional iris, which has a typical length less than half the large waveguide dimension. The coupling constant, which is a complex number, then in this case is nearly real and between zero and one in magnitude. The coupling constant approaches magnitude unity and the effective mutual

[1]The circuit of Fig. 6 is of a different form than any of the many coupled circuits in ref. 9.

coupling is positive real and approaches infinity as the resonance frequency of the iris approaches that of the LGR from above. However, when the resonance frequency of the iris is lower than the frequency of the LGR, which is true for a long iris of length comparable to the large waveguide dimension, Z_{iris} is capacitive. Then, depending on the value of L_e, the coupling constant can be either nearly imaginary and between zero and one in magnitude, or nearly real and between one and infinity in magnitude. For the long iris, the coupling constant is typically imaginary and of magnitude less than unity as discussed further below. The coupling constant approaches magnitude unity and the effective mutual coupling is negative real and approaches infinity as the iris resonance frequency approaches that of the LGR from below.

At critical coupling, it is commonly understood that the effective mutual coupling reactance ωM_{eff} is equal to the square root of the product of the primary and secondary resistances [9]. This is true when the primary reactance is negligible compared to the primary resistance. Most of Terman's analysis carries this assumption and also the additional constraint that the resonance frequencies of the primary and secondary are equal. Neither of these assumptions apply in our problem. From an analysis of the circuit of Terman (Sect. 3, Fig. 16 [which is not further analyzed there]), the effective mutual coupling is given by

$$\omega M_{eff} = \sqrt{R_P R_S \left[1+\left(\frac{\omega L_P}{R_P}\right)^2\right]}.$$

In terms of the present circuit values, this equation can be written

$$\omega M_{eff} = \sqrt{Z_0 R'_{LGR}\left(1+\frac{{X_{iris}}^2}{{Z_0}^2}\right)}. \tag{26}$$

The combination of Eqs. (26) and (25) results in one of impedance conditions for critical coupling, Eq. (D2). However, because R'_{LGR} is a function of frequency, Eq. (D2) can be satisfied at almost any frequency without achieving critical coupling. As discussed in the previous section and in Appendix D, the other condition, Eq. (D1), must simultaneously be met to achieve critical coupling. This additional constraint is not discussed in ref. 9.

At critical coupling, it is commonly understood that the coupling constant is equal to the reciprocal of the square root of the product of the primary and secondary *Q*'s [9]. This is not the case in the present problem because the primary and secondary reactances are not pure inductances. Since the primary resistance Z_0 is in parallel with the resonant iris circuit, Fig. 5 (b), the primary *Q* is given by

$$Q_P = \frac{2Z_0}{2\pi f_c\left(L_c \frac{5+\sqrt{21}}{21-3\sqrt{21}}\right)},$$

where f_c is the iris resonance frequency, Eq. (16), and the equivalent inductance of the primary is given by the term in parenthesis. This equivalent inductance was derived by equating the magnetic flux and energy at iris self-resonance to those of an equivalent parallel *L*-*C* circuit. The secondary circuit, which consists of the circuit of Fig. 6 with open input, is more complicated. Analysis of this circuit with zero resistances leads to an expression for the secondary resonance frequency f_S, which includes the presence of the iris. The expression was

found using Mathematica and is a solution to a quartic in f_S^2. The frequency can be evaluated and is a measure of the frequency at critical coupling f_m.[2] It is typically within 1% above or below the natural LGR resonance frequency, Eq. (6). An analysis of the stored magnetic flux and energy at this frequency can be used to obtain an equivalent secondary inductance L_S, and, with the resistances added to the circuit of Fig. 6, the dissipated power at this frequency leads to an equivalent resistance R_S. These in turn produce the secondary Q,

$$Q_s = \frac{2\pi f_s L_s}{R_s}.$$

This Q is typically within about 5% above or below the isolated LGR Q, Eq. (4).

3 Results

From the previous section, critical coupling between the LGR and waveguide is made by meeting two conditions. The first is the transformation of the LGR equivalent conductance from Eq. (1) into the waveguide characteristic admittance, Eq. (23). Due to the Lorentzian behavior of $G_{\mathrm{LGR}}(f)$, this condition is typically met through a frequency shift relative to the natural LGR resonance frequency. The LGR and sample geometry also strongly influence this condition. However, iris dimensions do not. The second condition is that the iris susceptance cancel the LGR susceptance, Eq. (1), as seen by the iris at this frequency shift, Eq. (24). Iris dimensions strongly influence only the second match condition.

The results are divided into four parts. First, we show details of the process of coupling between a WR-28 waveguide and the 3-loop-2-gap 10-mm-long Q-band LGR of dimensions shown in Table 1, made by irises of characteristically different dimensions, Table 2. It is found, for various iris types, that increasing the iris length or width increases the coupling strength, and increasing the thickness decreases the coupling strength in the circuit model, consistent with Ansoft HFSS simulations. For this study, the iris dimensions for the circuit model were chosen by first simulating the LGR, iris, and waveguide using the driven mode Ansoft HFSS. The dimensions used in the circuit model were exactly those required to achieve critical coupling in Ansoft HFSS. The flux occupation factor s, defined by Eq. (17), was then adjusted for critical coupling. Values that produced critical coupling for these two irises are shown in Table 2. They are different because of differences in the magnitude of magnetic flux from each iris relative to the flux in the LGR outer loop. It is found that $s \cong 0.2|\Phi e/\Phi c|$, where $\Phi_e = L_e i_o''$ and $\Phi c = L_c i_c$ (see Fig. 6). Although it is possible to obtain s strictly within the circuit model from the circuit currents by iteration, it is more practical to treat s as a matching parameter, similar to the adjustment of a tuning pill in a conventional iris tuning system.

From this study, we find that the magnitude of the frequency shift at match relative to the natural LGR resonance frequency is determined by the LGR and waveguide dimensions, not by the iris. In the remaining results, insights gained from the circuit model are used to explore the behavior of different iris types. In Sect. 3.2, we examine an iris with a self-resonance frequency close to the LGR and find that as the iris becomes resonant, the iris width must be made smaller to achieve critical coupling. Types of frequency pulling are discussed in Sect. 3.3 as are the advantages of the long (capacitive) iris over the conventional (inductive) iris because frequency shift due to sample size is opposite to the frequency shift due to iris tuning to accommodate reduced Q value. Finally, in Sect. 3.4, the circuit model is used to design a new LGR and coupler without frequency pulling. Results are consistent with finite element simulations.

3.1 Conventional vs. Long Iris

The admittance of the series combination of L_e and Z'_{LGR} as a function of frequency near the natural LGR resonance frequency for conventional and long irises is shown in Fig. 8. The Lorentzian and Lorentzian-derivative variation with frequency are due to G_{LGR} and B_{LGR}, respectively, Eq. (22). For any iris, match occurs when the LGR conductance is transformed to the reciprocal of the waveguide characteristic impedance, Eq. (23). Since the iris properties contribute only to the inductance ratio in Eq. (23), the transformation is largely accomplished through a frequency shift relative to the natural LGR resonance frequency. The frequency shift for the conventional iris, Figs. 8(a) and (b), is negative (-372 MHz, Table 2) because it has an inductive susceptance, which exactly cancels the LGR susceptance at this frequency shift, Eq. (24). In contrast, the long iris is capacitive, and so the frequency shift is positive (251 MHz, Table 2). Again, the iris susceptance exactly cancels the LGR susceptance, Eq. (24), that occurs when the LGR conductance is transformed to the reciprocal of the waveguide characteristic impedance, Eq. (23), except now on the other side of the Lorentzian peak. The amount of frequency shift predicted by the circuit model for both irises is within 20% of Ansoft HFSS.

For decreasing LGR Q, the Lorentzian in G_{LGR} becomes wider, and it is seen from Fig. 8(b) that the conventional iris will match at progressively lower frequencies. Because the real part of the sample dielectric constant also pulls the natural LGR resonance frequency down for increasing sample size, the two effects are additive and cause a large negative frequency difference between match without sample and match with sample, f_{mn}-f_{ms}. For the long iris, the opposite occurs: as the Lorentzian in G_{LGR} becomes wider, match appears at higher frequencies, Fig. 8(d), and sample presence pulls the natural resonance frequency down. The two effects tend to cancel, reducing f_{mn}-f_{ms}. This is consistent with Ansoft HFSS simulations.

In addition to the iris reactance type and frequency shifts, other properties of the conventional and long irises are complementary or dual. The coupling constant at match is nearly of unity magnitude for both irises, Table 2, but is positive real for the conventional and negative imaginary for the long. Ansoft HFSS simulations of the LGR and iris wall surface currents for the conventional and long irises are shown in Fig. 9. It is seen that the surface current at the end of the iris is significantly stronger for the conventional iris, Figs. 9(a) and (b). This iris also perturbs the LGR wall surface currents significantly more than the long iris. The magnetic field vector plots, Figs. 9(c) and (d), indicate a phase reversal of the iris currents relative to the inner loop LGR currents. These current properties and phase shifts are also reflected in the circuit model as indicated by the current ratios in Table 2. The currents are defined by the circuit of Fig. 6. The current at the inductive end of the iris relative to the intercepted outer loop current i_c/i''_o is five times stronger for the conventional iris than the long. This current also has nearly 90† phase shift for the conventional iris, whereas the long iris has almost no phase shift. Due to the definitions in Fig. 6, the absence of phase shift between the iris and LGR outer loop current components is reflected by a negative sign in the ratio. Therefore, the numbers in Table 2 show that the LGR wall current splits and flows around the outside of the conventional iris with a reversal in the center and a 90† phase shift. For the long iris, the LGR wall current comes together and flows primarily as displacement current across the middle of the iris with some counterflow at the ends. Very small phase shift is seen. The current i_{Cc} represents the (displacement) current through the center of the iris, capacitor C_c, and is given by $i_{cc}=i_{in} - i_{cc} - i''_o$. The overall current magnitude is about three times stronger for the conventional iris than the long. All of these observations are consistent with Ansoft HFSS simulations. The peak magnetic field strength in the iris as observed by Ansoft is also a factor of three larger for the conventional iris than the long. The observed fields are consistent with the conventional iris being primarily magnetic (inductive) and the long iris primarily electric (capacitive). The last three current ratios in Table 2 show the current in the LGR inner loop relative to the two outer loops and the input current. The conventional iris is seen to perturb

the outer loop current by about a factor of three more than the long and in the opposite way. Perhaps, surprisingly, both irises significantly perturb the flux symmetry between the outer loops. The last entry shows the level of flux magnification delivered by the LGR, which is the same for both irises as expected. The phase reversal shown between the inner loop and input current is consistent with the Ansoft HFSS magnetic field vectors shown in Figs. 9(c) and (d). The difference in currents between the long and conventional irises produces the difference in the rf magnetic energy density profile at the sample as shown in Fig. 2(a). The conventional iris degrades the uniformity by 8% while the long iris improves the uniformity by about 7%. The long iris thus gives an overall uniformity improvement of 15% over the conventional slotted iris.

3.2 Resonant Iris

An iris that produces match near its isolated self-resonance frequency, $f_0 \cong f_{c0}$ of Eq. (16) $\left(l_c \cong \frac{c}{2f_0}\right)$ has no unique properties because the presence of the LGR outer loop alters the resonance frequency of the iris due to the modification of the iris flux as described in Sect. 2.3. However, an iris that produces match near its self-resonance frequency in the presence of the LGR outer loop as computed from the circuit of Fig. 5(c) does have unique properties. As the iris self-resonance frequency approaches the match frequency ($l_c \cong 4.65$ mm for the LGR dimensions of Table 1), the iris width must be reduced by over an order of magnitude ($w_c \cong 8$ μ) to obtain critical coupling. The primary quality factor Q_P increases by an order of magnitude from order unity. The stored energy in the iris therefore increases. Sensitivity of match to percentage changes in the iris dimensions also increases. The amount of frequency shift relative to the natural LGR resonance frequency stays about the same, consistent with the first condition for match, Eq. (23). The iris reactance at match is also similar as required by Eq. (24).

A resonant iris has advantages, such as permitting iris location in weak field regions, but a different approach must be taken to reduce the frequency shift.

3.3 Frequency Pulling

The circuit model permits detailed analysis of frequency pulling, which can be defined as changes in frequency at match f_m with respect to changes in LGR resonance frequency f_0, resonator Q, or sample size a, which typically influences both f_0 and Q. As discussed in Sects. 2 and 3.1, the sign of $\Delta f = f_m f_0$ is equal to the sign of the iris susceptance. As shown in Table 2, the magnitude of Δf is comparable for the conventional and long irises, with the long iris a bit smaller due to its greater flux occupation factor, which reduces the admittance. The long iris has a $\partial f_m/\partial Q$ opposite the direction of $\partial f_0/\partial a$ due to the real part of the sample and sample holder dielectric constants, decreasing the difference in f_m with and without sample compared to the conventional iris. Perhaps, surprisingly, frequency shifts due to iris adjustments needed to accommodate changes in Q value can be larger than the corresponding LGR natural resonance frequency shifts due to sample size.

Differences in match frequency f_m at different LGR Q can be reduced by adjusting the LGR dimensions so that G_{LGR} meets Eq. (23) closer to the natural LGR resonance frequency f_0. This condition is where the normalized conductance is unity, Fig. 8. In the case of the 3-loop-2-gap LGR (Table 1 dimensions), *fm* can be put closer to f_0 by increasing the outer loop diameter relative to the inner loop diameter. Analysis of the crossings of the conductance curves for the Q values from 871 to 229 in Fig. 8(a) or (c) shows that the variation in match frequency over the range of these Q values can be reduced to 8.5 MHz, compared with the excursion of —180 MHz for the conventional iris and +115 MHz for the long iris as shown in Figs. 8(b) and (d), respectively. If the LGR geometry is designed so that G_{LGR} satisfies Eq. (23) where the conductance curves for two particular Q values cross, then the match frequency is identical for

these two Q values. Similarly, the LGR geometry can be designed so that G_{LGR}meets Eq. (23) where $\partial fm\ \partial Q$ is nulled for changes in Q about any particular Q value. Then, the match frequency is invariant for small changes in Q about that particular Q value. These predictions have been validated by Ansoft HFSS simulations. Practical resonator design must also accommodate changes in f_0 due to sample. This is discussed further in the next section.

The circuit model also shows that the match frequency can be made fixed over large Q variations by the adjustment of an element that changes the natural LGR resonance frequency f_0 in addition to the adjustment of the iris dimensions. However, a more attractive and novel alternative is to match at precisely f_0, which, from Fig. 8(a) or (c), requires a constant iris susceptance and an adjustment of the LGR conductance G_{LGR}. Changing the LGR conductance is not possible through a typical reactive iris, and, therefore, another form is needed, for example, something that varies the LGR magnetic flux near the iris or changes the transmission line characteristic impedance. There could be an EPR signal-to-noise ratio benefit with this coupling method.

3.4 LGR Design for Reduced Frequency Pulling

The predictions of the circuit model were used to design a new LGR in Ansoft HFSS. Starting from the 10-mm-long 3-loop-2-gap LGR and a sample of the dimensions shown in Table 1, the inner loop radius was decreased to 0.234 mm and the outer loop radius was increased to 1.905 mm. This should increase the equivalent resistance as seen by the iris and place match closer to the natural resonance frequency. As predicted by the circuit model, the width of the long iris increased to 2.16 mm to produce match. This is a surprisingly large iris opening, more than half the waveguide width. The Q of the LGR decreased to 125. The match frequency was 140 MHz above f_0. The magnetic field energy density profiles on the LGR axis for eigenmode and driven solutions are shown in Fig. 2(b). The eigenmode uniformity is significantly improved over the unmodified LGR due to the smaller inner loop. The iris further improves the uniformity, like the previous long iris; however, the difference is much smaller, consistent with a smaller iris perturbation. The lower the $\Delta f = f_m - f_0$, the lower the perturbation of the mode by the iris relative to the eigenmode solution. The difference in flux between the coupled outer loop and the uncoupled outer loop is reduced. Magnetic field uniformity can be further trimmed using the techniques of ref. 11. These techniques are more easily applied when the iris has a smaller perturbation on the resonator.

A thin metallic baffle of 0.1-mm thickness, 1.72-mm width, and 7.22-mm length was inserted into the iris opening to reduce coupling when the sample was removed. Consistent with the circuit model, the difference in f_m with and without sample was only 20 MHz. Thus, frequency pulling relative to changes in sample can be eliminated with an appropriate LGR and iris design.

4 Summary

In electrical engineering, lumped *R-L-C* models work well when characteristic dimensions of the structure to be modeled are much less than a wavelength. Similarly, distributed circuit models based on analytical solutions to Maxwell's equations are useful when characteristic dimensions are similar or greater than a wavelength. In this latter situation, lumped circuit models can also be selectively used [8,12,14]. Computer-based finite element modeling provides rigorous solutions but can be criticized because the insight provided by analytic solutions is lost. In this paper, we have developed an *R-L-C* model for a problem that falls in an intermediate wavelength range. Finite element modeling was used not only in the development but also for validation of the *R-L-C* model.

The rationale for this paper is the physical insight that the *R-L-C* model provides in describing microwave coupling from a waveguide to an LGR. Q-values of the primary (waveguide and

iris) and secondary (iris and LGR) are low and resonance frequencies disparate, so approximations customarily made in the analysis of coupling to high-*Q* cavities are no longer appropriate. The analysis has been carried out with and without an aqueous sample. Adjustment between these states was modeled by changing the iris dimensions or by placement of a metallic baffle in the iris (Sect. 3.4). More typically, a secondary circuit is introduced between the iris and waveguide and often takes the shape of a moveable metallic pill. If the iris and LGR are properly designed, this secondary circuit introduces a straightforward transformation of the complex impedance. It has not been explicitly considered in the present analysis and is the subject for a future investigation. Preliminary observations using Ansoft HFSS suggest that the movement of a given-size pill across the waveguide width can accommodate a larger LGR *Q* variation when used with the long iris than the conventional iris. The *R-L-C* model was valuable, and perhaps essential in providing insight into the design of the coupler.

The iris produces critical coupling in an analogous way to a basic single-stub or slide-screw tuner [15]. Critical coupling is accomplished in two parts. First, the length of transmission line between the mismatched load and the stub provides a rotation on the admittance chart from the normalized load admittance to the normalized $G = 1$ circle. The rotation is about the center of the chart. Second, the normalized susceptance component of the load admittance at this point is canceled by the pure susceptance of the stub, producing critical coupling. It is necessary to place the stub at $G = 1$ so that the stub can have a pure susceptance. (A stub conductance will cause power loss.) The stub tuner theoretically produces critical coupling with no frequency shift, $f_m = f_0$.[3]. In the case of the iris, critical coupling is also a two-part process. However, the rotation from the normalized load admittance to the normalized $G = 1$ circle, Eq. (23), is accomplished by a frequency shift relative to the LGR natural resonance frequency through the Lorentzian behavior of $G_{LGR}(f)$. The rotation is about a point other than the center of the Smith chart and is related to the LGR outer loop inductance, Eq. (24). The rotation to the normalized $G = 1$ circle determines the frequency at which critical coupling occurs. The second part of critical coupling, the cancellation of the normalized susceptance component of the LGR admittance at this point by the pure susceptance of the iris, Eq. (24), is accomplished by the iris in the same way as the stub tuner.

The long iris has benefits over the conventional iris for the EPR spectroscopist. These include improved rf magnetic field uniformity at the sample and reduced frequency pulling. The long iris has also been used to match cavities. Other shapes of irises can be modeled using the circuit model with appropriate modification of the reactive elements with the iris dimensions. The model led to the design of an LGR with unusually large outer loops and an unusually large iris, which are critically coupled close to the natural LGR resonance frequency. The circuit model can be used to explore a wide range of parameter space outside the range of conventional thinking. Typically, the circuit model would be used to guide, and not replace, the use of a finite element code. For the cases presented here, when the dimensions predicted by the circuit model were used in the finite element code, critical coupling was sufficiently close that reasonably small changes in iris dimensions were required to obtain critical coupling. Exact iris and LGR dimensions, typically produced using electric discharge machining (EDM) or laser milling, would be determined by finite element modeling at the final stages of design.

Acknowledgements

This work was supported by grants EB001417, EB001980, and EB002052 from the National Institutes of Health.

[3]However, in practice, a transition is needed to provide a connection between the resonator and the transmission line. This transition will act like an iris.

Appendix A: Relationship between self and mutual inductance example

The cross-section of a long solenoid inside a metallic shield is shown in Fig. 10. Figure 10(a) represents a low-frequency limit where the coil thickness is much less than the skin depth, and Fig. 10(b) shows a high frequency limit where the coil thickness is much larger than the skin depth. We present three treatments leading to the same analytic expression for the self-inductance of the inner coil in the presence of the shield. The first closely follows Bogle [16] and is a low frequency treatment involving magnetic flux conservation in the shield without consideration of mutual inductance. The accuracy of the self-inductance expression in various limits is extensively discussed by Bogle. The second is also a low frequency treatment but explicitly treats the mutual inductance between the shield and the coil. The third is a high frequency limit that permits the separation of the total current on the inner coil into an inner surface current and an outer surface current. This leads to the total self-inductance of the coil expressed by two self inductances connected in parallel with no mutual coupling. The results are consistent with a statement by Grover [10]: “Self-inductance is merely a special case of mutual inductance.” The presentation shows, for this particular case, that the metallic wall rf boundary condition can be used to define surface currents and distinct regions, which permits the shielded coil to be separated into two self-inductances connected in parallel. In this paper, this approach includes capacitances and resistances and is applied to the coupled iris-LGR.

In Fig. 10(a), there is a total azimuthal current i uniformly distributed along a total length l and an induced uniformly distributed total current I in the shield. Ampere's law can be used to relate the current to the magnetic field between coil and shield, $H_o = I/l$, and inside the coil, $H_i = (i - I)/l$. The magnetic field inside the coil is reduced by the shield current. Then, the total magnetic flux between shield and coil is $\Phi_o=\mu_0\pi\left(r_0{}^2 - r_i^2\right) I/l$, and inside the coil, $\Phi_i=\mu_0\pi r_i^2\,(i - I)\,/l$. In order for the total magnetic flux in the shield to be zero, these two fluxes must be equal; this yields a relationship between the coil and shield currents,

$$I=\frac{r_i{}^2}{r_o{}^2}i. \tag{A1}$$

This equation can be substituted into the equation for Φ_i, and the self-inductance of the coil in the presence of the shield $L = \Phi_i/i$ can be written as

$$L=\frac{\mu_0\pi r_i{}^2}{l}\left(1 - \frac{r_i{}^2}{r_o{}^2}\right). \tag{A2}$$

This equation, which is consistent with Bogle [16], indicates that the shield reduces the self-inductance of the coil.

The same equation can be obtained by considering a mutual inductance between shield and coil. Following the definition of mutual inductance, the total emf induced in the coil can be written as

$$V=L_i\frac{di}{dt} - M\frac{dI}{dt}, \tag{A3}$$

where $L_i=\mu_0\pi r_i^2/l$ is the ratio of the flux in the coil produced by the coil current i to the coil current i, and $M=\mu_0\pi r_i^2/l$ is the ratio of the flux in the coil produced by the shield current I to the shield current I. Therefore, Eq. (A3) can be written as

$$V=\frac{\mu_0\pi r_i^2}{l}\frac{d\,(i-I)}{dt}=\frac{\mu_0\pi r_i^2}{l}\left(1-\frac{r_i^2}{r_o^2}\right)\frac{di}{dt}, \tag{A4}$$

where the last step was obtained by substituting Eq. (A1). Therefore, the equivalent self-inductance of the coil is given by the term in front of the last time derivative, which matches Eq. (A2).

In the high frequency limit where the coil thickness is much larger than the skin depth, the rf magnetic field inside the metal is equal to zero [8]. Thus, Ampere's law can be used to relate the magnetic field just outside the metal to the surface current. Between shield and coil, $H_o = I/l$. Because this magnetic field is uniform between shield and coil, there is a current on the outside surface of the coil as shown in Fig. 10(b) and is given by $H_o = i_o/l$. Therefore, $i_o = I$. On the inside surface of the coil, $H_i = i_i/l$. The metallic wall rf boundary condition permits the separation of the coil into two parts. We can consider the self-inductance of the inner part of the coil $L_i = \mu_0\pi r_{i1}{}^2/1$ as the ratio of the flux inside the coil produced by the current i_i to i_i, and the self-inductance of the outer part of the coil $L_o = \mu_0\pi\,(r_{i2}{}^2 - r_o{}^2)/l$ as the ratio of the flux outside of the coil produced by the current i_o to i_o. Because the total current of the coil is the sum of the inner and outer currents, $i = i_i + i_o$, the emf induced by the inner self-inductance is

$$V=\frac{\mu_0\pi r_i^2}{l}\frac{di_i}{dt}=\frac{\mu_0\pi r_i^2}{l}\frac{d\,(i-I)}{dt}=\frac{\mu_0\pi r_i^2}{l}\left(1-\frac{r_i^2}{r_o^2}\right)\frac{di}{dt}, \tag{A5}$$

where we have assumed $r_{i1} \cong r_{i2} \cong r_i$ and used Eq. (A1) to obtain the last step. This emf is the same as that developed by the total self-inductance of Eq. (A4). Equation (A5) indicates that the effect of the mutual inductance of the shield on the coil can be considered to be the induction of a current flowing on the outside of the coil i_o and a reduction of the current flowing on the interior of the coil i_i relative to the total. It can also be shown that the emf of Eq. (A5) is the same as that developed by the outer self-inductance,

$$V=\frac{\mu_0\pi\left(r_o^2-r_i^2\right)}{l}\frac{di_o}{dt}=\frac{\mu_0\pi\left(r_o^2-r_i^2\right)}{l}\frac{dI}{dt}=\frac{\mu_0\pi r_i^2}{l}\left(1-\frac{r_i^2}{r_o^2}\right)\frac{di}{dt},$$

where again we have used Eq. (A1). That the emfs are equal indicates that a gap cut in the wall of the coil to form a capacitor for an LGR will not disturb the current distribution between the inside and outside of the LGR. It can also be shown that the total self-inductance L of the coil for the total current i is the parallel combination of L_i and L_o,

$$L=\frac{1}{\frac{1}{L_i}+\frac{1}{L_o}}=\frac{1}{\frac{l}{\mu_0\pi r_i^2}+\frac{l}{\mu_0\pi\left(r_o^2-r_i^2\right)}}=\frac{\mu_0\pi r_i^2}{l}\left(1-\frac{r_i^2}{r_o^2}\right),$$

with no mutual inductance between them. Such an LGR can be viewed as a capacitor receiving the total current i from the two inductors in parallel.

Appendix B: LGR lumped circuit values at cutoff

In Ref. [11], Mett et al. present a lumped circuit model and the corresponding lumped circuit values of inductance, resistance, and capacitance of an LGR at high frequencies. The values are functions of the LGR dimensions and conductivity and do not include effects of sample. The circuit model is for the LGR at cutoff where the fields are axially uniform. Mett et al. also present a transmission line model that accounts for the deviation of the LGR resonance frequency from cutoff and a corresponding axial non-uniformity of the LGR fields produced by a loading of the LGR by an impedance at the LGR ends. Results are compared to finite element simulations and agreement is good, for both a long LGR with a length of about one free space wavelength and a short LGR with a length of 12% of the free space wavelength. The impedance of the ends of the LGR is found to perturb the resonance frequency of the short LGR more than the long (3.4% vs. 1.0% from cutoff), whereas the axial field non-uniformity is more apparent in the long LGR. This type of non-uniformity can be eliminated by an end design that presents an rf open impedance to the LGR ends. Then, the LGR resonates at its cutoff frequency.

At cutoff, the LGR rf currents are transverse and can be considered to flow on the interior metal surfaces of the LGR (see Fig. 1), penetrating to a depth of one skin depth [8],

$$\delta=\frac{1}{\sqrt{\pi f\mu_0\sigma}},$$

where the frequency $f = \omega 2\pi$,μ_0 is the magnetic permeability of free space, and σ is the conductivity of the metal. We assume that the LGR has an axial length l with m equal gaps of thickness t and width w with a single inner loop of radius r_i and m equal loops of radius r_o (in Fig. 1, $m = 2$). Similar to the configuration in Appendix A, the magnetic flux in the inner loop returns in the outer loops. Each LGR gap is a capacitor fed by a self-inductive loop on each of its two ends. Using the metallic wall rf boundary condition to define the current in each loop, the self-inductance of each loop is given by

$$L=\frac{\mu_0\pi r^2}{l}, \tag{B1}$$

where r is the respective loop radius. However, since the rf current enters each gap end, there is an additional self-inductance caused by the resulting magnetic flux in each gap end. Jackson [12] shows that the self-inductance of a set of parallel plates of dimensions equal to the gap dimensions and fed from one end is given by

$$L=\frac{\mu_0 tw}{3l}, \tag{B2}$$

which is one-third the self-inductance of the plates shorted at the end opposite the feed. In the case of the LGR, the gap is fed from both ends, and there is an rf current null between them at a location that depends on the relative sizes of the self-inductances on each end. The location of the null can be found by using the null to separate the gap into two parts—one that feeds rf current to the outer loop and one to the inner loop. Like the example shown in Appendix A, the loop voltage on each side of the rf current null is the same and the two parts are in parallel. Since the resonance frequency of each part is the same, we find (for m gaps),

$$f=\frac{1}{\sqrt{L_o C_o}}=\frac{1}{\sqrt{(L_i/m)\,C_i}}, \tag{B3}$$

where, using Eqs. (B1) and (B2),

$$L_o=\frac{\mu_o}{l}\left(\pi {r_o}^2+\frac{tw_o}{3}\right),$$

$$\frac{L_i}{m}=\frac{\mu_0}{l}\left(\frac{\pi {r_i}^2}{m}+\frac{tw_i}{3}\right),$$

with $w = w_o + w_i$, and we tentatively take $C_o=\frac{\varepsilon_0 w_o l}{t}$ and $C_i=\frac{\varepsilon_0 w_i l}{t}$. If we assume the selfinductance of the gap is small compared to the loops, Eq. (B3) results in the relationship

$$\frac{w_i}{w_o}=\frac{{r_o}^2}{{r_i}^2/m}.$$

This relationship can be used to write the total self-inductance of the loop and partial gap as

$$L_o=\frac{\mu_0}{l}\left(\pi {r_o}^2+\frac{tw}{3}\frac{{r_i}^2/m}{{r_o}^2+{r_i}^2/m}\right), \tag{B4}$$

$$L_i=\frac{\mu_0}{l}\left(\pi {r_i}^2+\frac{mtw}{3}\frac{{r_o}^2}{{r_o}^2+{r_i}^2/m}\right). \tag{B5}$$

These equations are the same as those presented by Mett et al. [11].

As described by Mett et al. [11], the total capacitance of each gap is increased by a factor γ by the fringing field that has been quantified by an exact two-dimensional electrostatic solution derived from conformal mapping techniques [13],

$$C\prime=\gamma\frac{\varepsilon_0\, wl}{t},$$

where the dimensionless factor γ is given by

$$\gamma=\frac{tK(\kappa)}{wK\left(\sqrt{1-\kappa^2}\right)}. \tag{B6}$$

Here, *K* represents the complete elliptic integral of the first kind, and the parameter κ in the arguments of the elliptic integral is a real number between zero and one determined by solving the equation,

$$\frac{w}{t}=\frac{K(\kappa)\,E\left\{\arccos\left[\frac{E(\kappa)}{K(\kappa)}\right],\kappa\right\}-E(\kappa)\,F\left\{\arccos\left[\frac{E(\kappa)}{K(\kappa)}\right],\kappa\right\}}{E(\kappa)\,K\left(\sqrt{1-\kappa^2}\right)-\left(\frac{\sqrt{1-\kappa^2}}{\kappa}\right)^2 E\left(\sqrt{1-\kappa^2}\right)K(\kappa)}. \tag{B7}$$

In this equation, E of single argument represents the complete elliptic integral of the second kind while E of double argument represents the elliptic integral of the second kind. Also, F represents the elliptic integral of the first kind. Equation (B7) was solved numerically and Eq. (B6) evaluated using Mathematica.

Finally, based on the metallic wall rf boundary condition, which relates the magnetic field to the surface current, the resistance of each LGR loop plus partial gap (see Eqs. (B4) and (B5)) was found by scaling $1/\sigma$ by the length of the current path divided by the cross-sectional area of the current path $l\,\delta$. The length of the current path is the circumference of the loop less the gap thickness plus twice the effective gap inductance gap width $w_o/3$ or $w_i/3$ since the current flows oppose across the vacuum gap,

$$R_o=\frac{1}{\sigma l\delta}\left(2\pi r_o-t+\frac{2w}{3}\frac{r_i^2/m}{r_o^2+r_i^2/m}\right), \tag{B8}$$

$$R_i=\frac{1}{\sigma l\delta}\left(2\pi r_i-mt+\frac{2mw}{3}\frac{r_o^2}{r_o^2+r_i^2/m}\right). \tag{B9}$$

These equations differ from those presented by Mett et al. in the gap thickness correction and have been found to give Q values (through Eqs. (2)-(4) of the main text) about three times more accurate (within 1.5% instead of 5% of Ansoft HFSS values) than without this correction.

Appendix C: Circuit equations

A complete set of circuit equations for the half-circuit of Fig. 6 is derived from the defined mesh currents and component voltage drops given by

$$v_{in}=\frac{i_{in}-i_{cc}-i_o''}{j\omega C_c}, \tag{C1}$$

$$v_{in}-v_{cc}=j\omega L_{cc}i_{cc},$$

$$v_{cc}=\frac{i_{cc}-i_c}{j\omega C_{cc}},$$

$$v_{cc}=j\omega L_c i_c,$$

$$v_{in} - v_l = (j\omega L_e + R_e)\, i_o'',$$

$$v_r = 2\,(j\omega L_o + R_o)\, i_o',$$

$$v_r = \frac{2\,(i_i - i_o')}{j\omega C'},$$

$$v_l - v_r = 2\,(j\omega L_i + R_i)\, i_i,$$

$$v_l = \frac{2\,(i_o - i_i)}{j\omega C'},$$

$$v_l = (j\omega L_e' + R_e')\left(i_o'' - i_o\right),$$

where C_{cc} and L_{cc} are given by Eqs. (12) and (13). Since there are 11 voltage and current quantities and 10 equations, the ratio between any two of these quantities is found by solving the system of equations for one quantity in terms of the other (e.g., using Mathematica).

Match is obtained when the input impedance given by Eq. (14), with the set of circuit equations, is near the characteristic impedance of the waveguide. The waveguide characteristic impedance for a TE_{10} mode in rectangular waveguide is given by [8]

$$Z_0 = \frac{\eta}{\sqrt{1 - \left(\frac{c}{2af}\right)^2}}, \tag{C2}$$

where η is the impedance of free space $\sqrt{\mu_0/\varepsilon_0}$ and a is the large dimension of the waveguide.

If a length of waveguide l_g exists between the iris and the input port, the input impedance is transformed by the waveguide according to

$$Z_{inl} = Z_0 \frac{Z_{in} \quad \cos\left(kl_g\right) + jZ_0 \quad \sin\left(kl_g\right)}{Z_0 \quad \cos\left(kl_g\right) + jZ_{in} \quad \sin\left(kl_g\right)},$$

where the waveguide wavenumber for a TE_{10} mode in rectangular waveguide is

$$k = \frac{2\pi f}{c}\sqrt{1 - \left(\frac{c}{2af}\right)^2}.$$

These equations were used to compare the impedances predicted by the circuit model near match to Ansoft HFSS.

Appendix D: Impedance at critical coupling

In terms of the iris-modified LGR impedance Z'_{LGR} defined in Fig. 6, equating the input impedance to the waveguide characteristic impedance yields a relationship between the bridge element L_e value, the real and imaginary parts of Z'_{LGR}, and the waveguide characteristic impedance,

$$X'_{LGR} = -\frac{1}{2}\omega L_e \pm \sqrt{R'_{LGR}\left(Z_0 - R'_{LGR}\right)}, \tag{D1}$$

and the and a value for the iris reactance from Eq. (15) in terms of the real part of Z'_{LGR} and the waveguide characteristic impedance,

$$X_{iris} = \pm \frac{Z_0}{\sqrt{\frac{Z_0}{R'_{LGR}} - 1}}. \tag{D2}$$

The iris-modified LGR resistance and reactance can be expressed in terms of the real and imaginary parts of the pure LGR impedance *ZLGR*, Eq. (1), as

$$R'_{LGR} = \frac{\left(\frac{1}{2}\omega L'_e\right)^2 R_{LGR}}{{R_{LGR}}^2 + \left[X_{LGR} + \omega\left(\frac{L'_e}{2} - L_o\right)\right]^2}, \tag{D3}$$

$$X'_{LGR} = \frac{1}{2}\omega L'_e - \frac{\left(\frac{1}{2}\omega L'_e\right)^2 \left[X_{LGR} + \omega\left(\frac{L'_e}{2} - L_o\right)\right]}{{R_{LGR}}^2 + \left[X_{LGR} + \omega\left(\frac{L'_e}{2} - L_o\right)\right]^2}. \tag{D4}$$

Equations (D1) and (D2) are the two conditions needed for critical coupling, and Eqs. (D3) and (D4) relate the iris-modified LGR impedance to the pure LGR impedance. In these equations, we have neglected terms of order $\frac{R_o}{\omega L_o}$, $\frac{R_e}{\omega L_e}$, and $\frac{R'_e}{\omega L'_e}$, which is a good approximation. The LGR dimensions and sample determine R_{LGR} and X_{LGR}, and the iris dimensions determine Z_{iris} and how L_o is split between L_e and L'_e, Eqs. (17) and (18). Both the real and imaginary parts of the LGR impedance are strongly frequency dependent and must be determined from Eq. (1). Very near the natural resonance frequency of the LGR, Eq. (6), X_{LGR} is typically on the order of an Ohm and R_{LGR} is close to the equivalent resistance given by Eq. (3). For a fixed LGR *Q*, the value of R_{LGR} increases as the ratio of the outer loop to inner loop cross-sectional area increases. Because of this, the behavior of the iris changes with LGR dimensions. For a given LGR and a given iris length, it is usually possible to adjust the iris width to produce match; larger width increases coupling strength. The match is typically achieved with nonzero LGR reactance and therefore a frequency deviation from the natural LGR frequency. The direction and amount of frequency shift, along with other types of iris behavior, depend on the iris dimensions as further discussed in Sect. 3.

References

1. Mett RR, Hyde JS. Rev. Sci. Instrum 2005;76:014702.
2. Froncisz W, Hyde JS. J. Magn. Reson 1982;47:515–521.
3. Hyde, JS.; Froncisz, W. Advanced EPR: Applications in Biology and Biochemistry. Hoff, AJ., editor. Elsevier; Amsterdam: 1989. p. 277-306.
4. Rinard, GA.; Eaton, GR. Biological Magnetic Resonance, Volume 24: Biomedical EPR -Part B: Methodology and Instrumentation. Eaton, SS.; Eaton, GR.; Berliner, LJ., editors. Kluwer Academic/ Plenum Publishers; New York: 2004. p. 19-52.
5. Froncisz W, Oles T, Hyde JS. Rev. Sci. Instrum 1986;57:1095–1099.
6. Klug CS, Camenisch TG, Hubbell WL, Hyde JS. Biophys. J 2005;88:3641–3647. [PubMed: 15749769]
7. Ginzton, EL. Microwave Measurements. McGraw-Hill; New York: 1957.
8. Ramo, S.; Whinnery, JR.; Van Duzer, T. Fields and Waves in Communication Electronics. Vol. 2nd edn.. Wiley; New York: 1984. sects. 4.12, 7.11, 10.12, 11
9. Terman, FE. Radio Engineers' Handbook, sects. 2, 3. McGraw-Hill; New York: 1943.
10. Grover, FW. Inductance Calculations. Van Nostrand; New York: 1946. p. 3
11. Mett RR, Sidabras JW, Hyde JS. Appl. Magn. Reson 2007;31:571–587.
12. Jackson, JD. Classical Electrodynamics. Vol. 2nd edn.. Wiley; New York: 1975. sect. 8.2, problems 6.5, 6.14
13. Smythe, WR. Static and Dynamic Electricity. Vol. 2nd edn.. McGraw-Hill; New York: 1950. chapter IV, problem 59
14. Marcuvitz, N., editor. Waveguide Handbook, chapters 5, 8. Boston Technical Publishers; Lexington, MA: 1964.
15. Brown, RG.; Sharpe, RA.; Hughes, WL.; Post, RE. Lines, Waves, and Antennas: The Transmission of Electric Energy. Vol. 2nd edn.. Wiley; New York: 1973. chapter 4
16. Bogle AG. Journal I. E. E 1940;87:299–316.

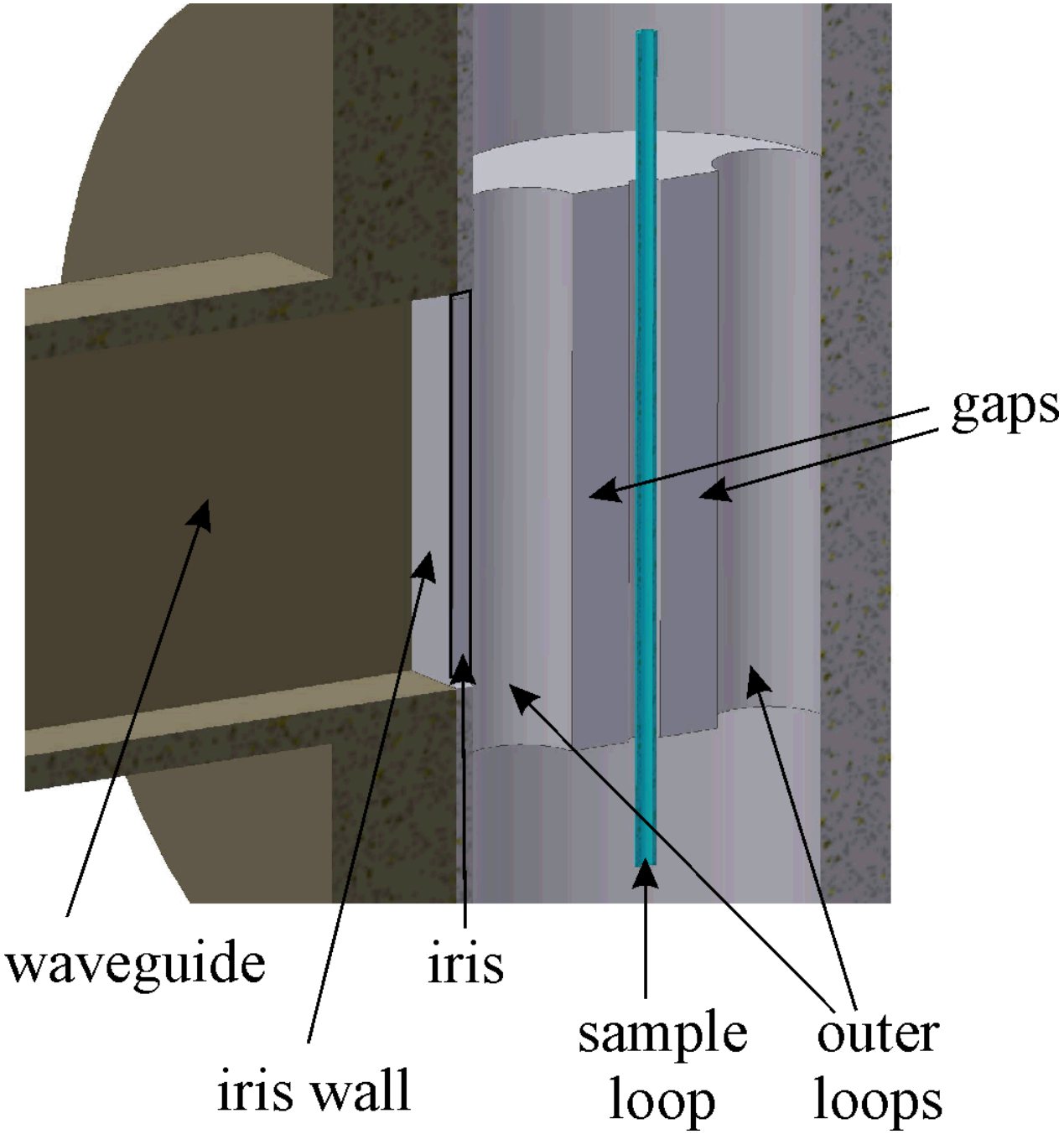

Fig. 1.
Mechanical drawing of bisected 10-mm-long Q-band 3-loop-2-gap LGR. Resonator body is shown in gray and the sample tube in blue. Gaps face bisecting plane. Coupling iris slot appears on nearest edge.

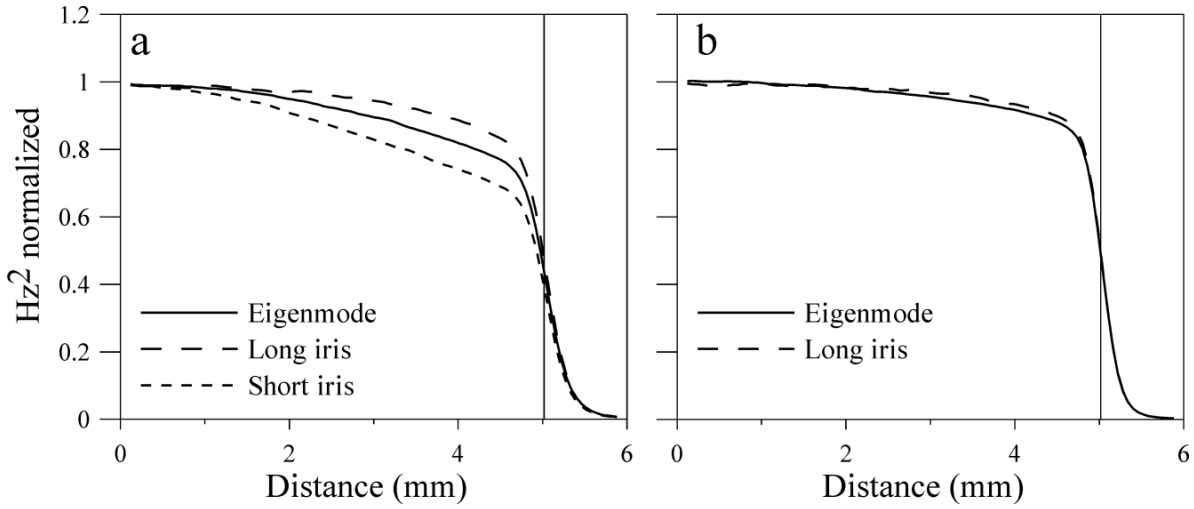

Fig. 2.

Radio frequency magnetic field energy density profile at sample center and LGR axis as predicted by Ansoft HFSS. Solid line indicates eigenmode (no iris) solution. Short dashes indicate conventional iris and long dashes long iris. **a** Iris and LGR dimensions shown in Tables 1 and 2. **b** LGR and iris dimensions modified from those in Tables 1 and 2 to reduce differences in match frequency with and without sample as described in Sect. 3.4. Modified dimensions: LGR inner loop diameter 0.467 mm, outer loop diameter 3.81 mm, long iris width 1.00 mm.

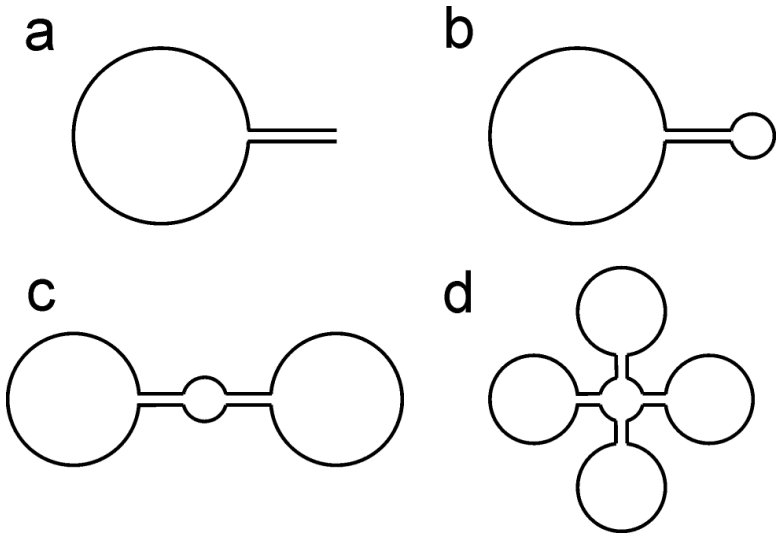

Fig. 3.
LGR cross-sections. **a** 1-loop-1-gap, no return flux loop. **b** 1-loop-1-gap. Sample is placed in smaller loop and larger loop is flux return path. **c** 3-loop-2-gap. **d** 5-loop-4-gap.

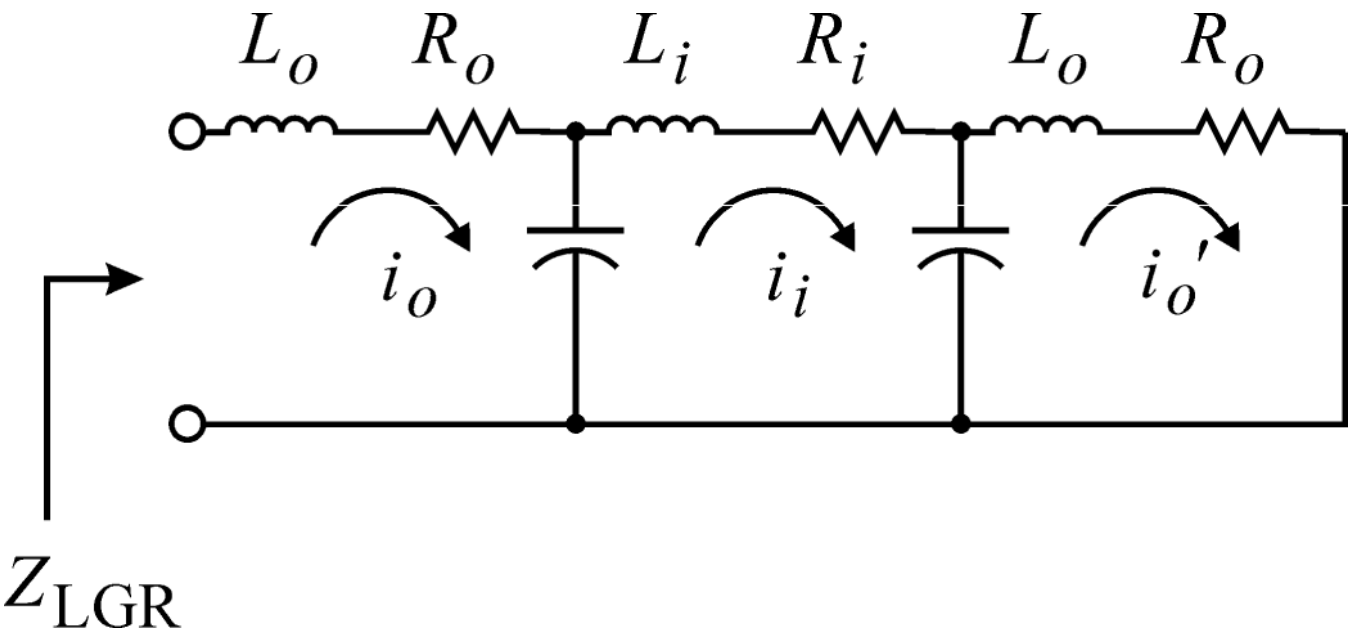

Fig. 4.
LGR circuit with driving point at fully broken outer loop.

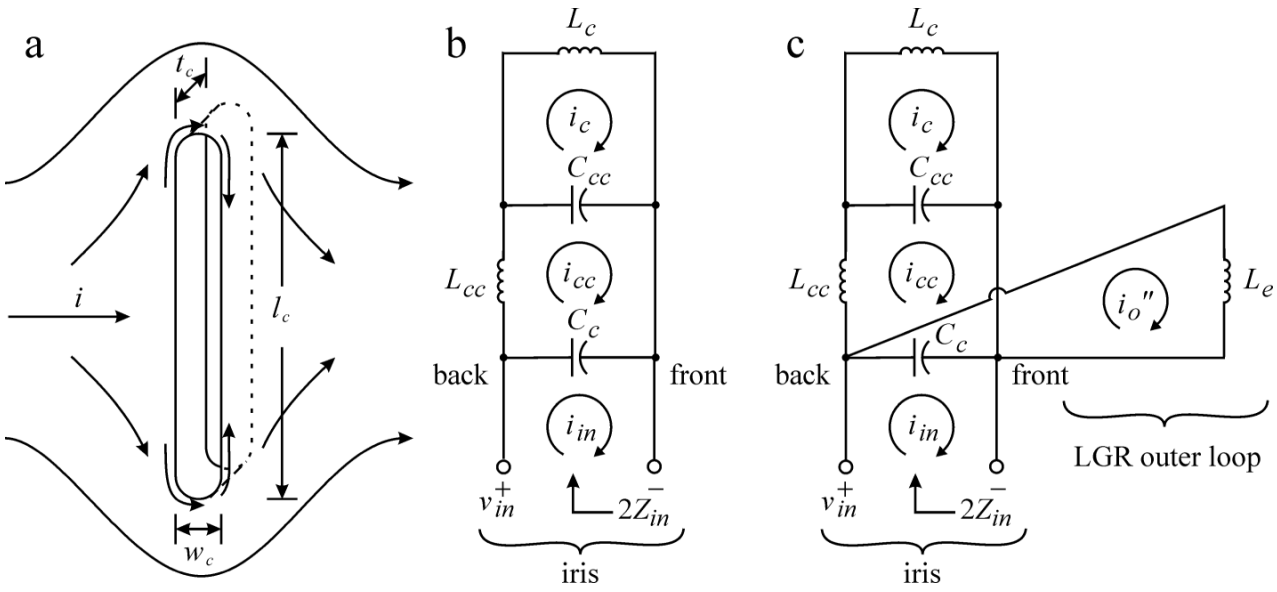

Fig. 5.

Iris **a** drawing showing qualitative current flow, **b** isolated iris half-circuit, **c** half-circuit of iris in proximity to LGR outer loop.

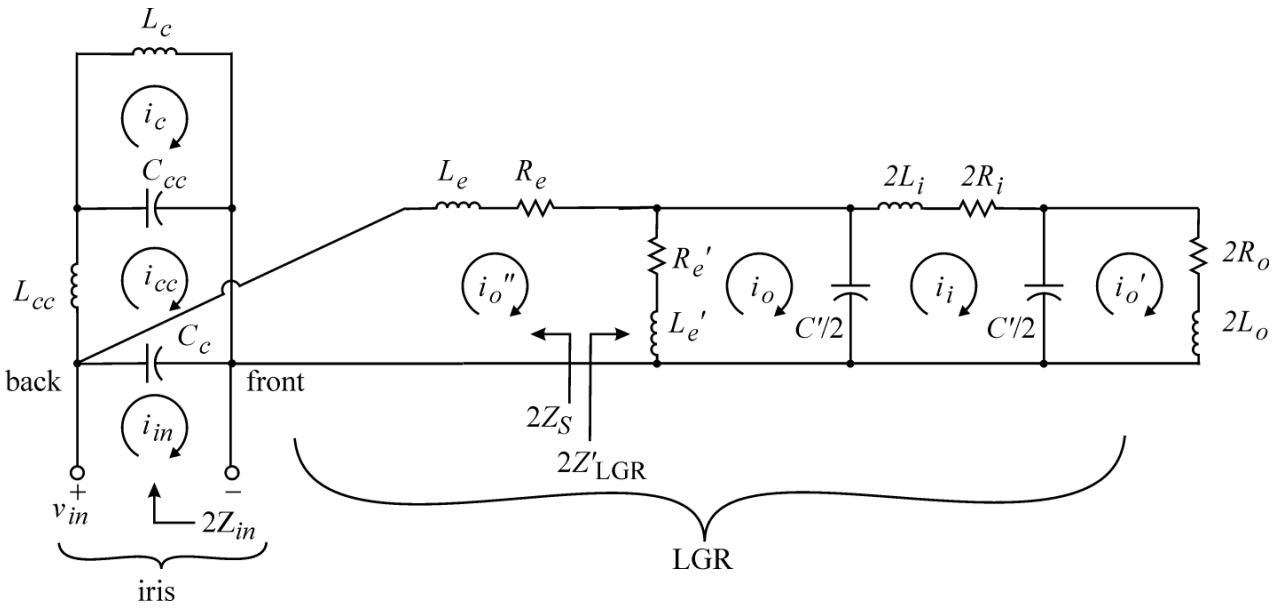

Fig. 6.
Half-circuit of connected iris and LGR.

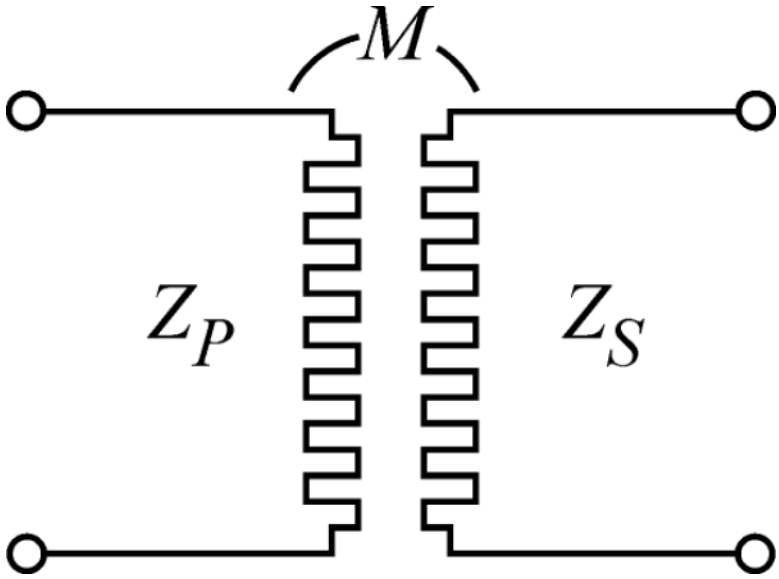

Fig. 7.
Generalized coupled circuit equivalent form [9].

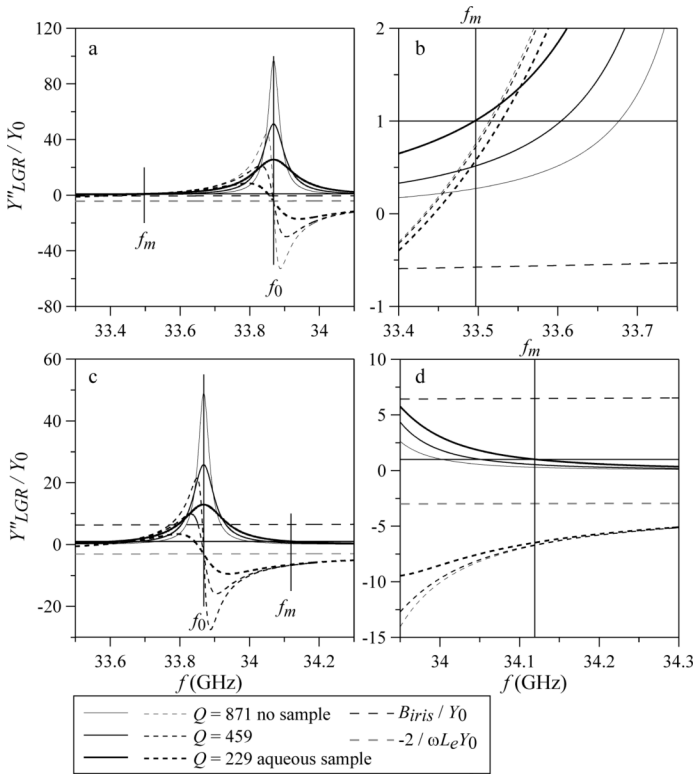

Fig. 8.

Admittance of the series combination of L_e and Z'_{LGR}, Eq. (22), as a function of frequency near the natural LGR resonance frequency and match. Also shown are the iris and outer loop admittances. Parts **a** and **b** correspond to a conventional iris, and parts **c** and **d** to a long iris, dimensions shown in Table 2. Parts **b** and **d** are expanded views of **a** and **c**, respectively. Solid lines are conductance and dashed lines are susceptance.

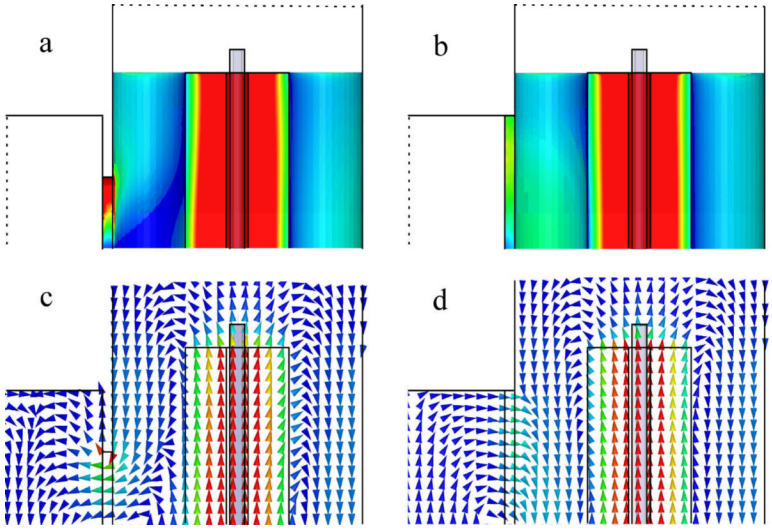

Fig. 9.

Wall surface current magnitude **a**, **b** and magnetic field vectors at symmetry plane **c,d** of 3-loop-2-gap LGR of dimensions and sample size given in Table 1, $Q = 229$, matched to WR-28 waveguide by conventional **a,c** and long **b,d** irises of dimensions shown in Table 2. Red to blue indicates maximum to minimum intensity.

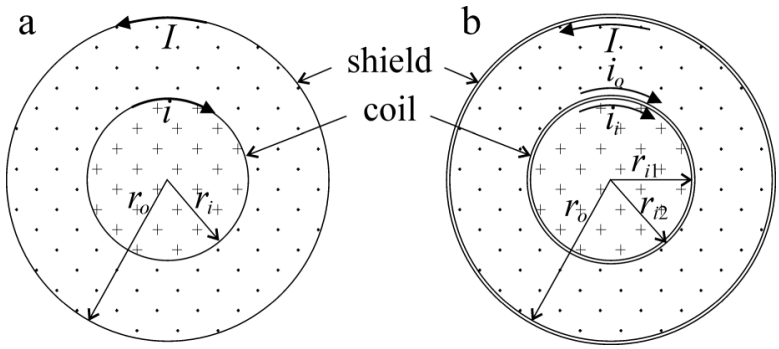

Fig. 10.

Shielded coil. Dots represent rf magnetic field directed out of page, and plusses represent rf magnetic field going into page. **a** Low frequency limit where rf skin depth is much greater than coil thickness. **b** High frequency limit where rf skin depth is much smaller than coil thickness.

Table 1

LGR properties and sample dimensions (mm).

sample radius r_s	0.127
sample tube outer radius r_t	0.165
inner loop radius r_i	0.330
outer loop radius r_o	1.030
length l	10.03
gap width w	1.156
gap thickness t	0.165
natural resonance frequency f_0 (GHz)	33.869
quality factor, no sample Q_{ns}	871
quality factor with sample Q_s	229

Table 2

Coupled LGR-iris properties.

	conventional	long
iris wall thickness t_c(mm)	0.305	0.305
iris opening width w_c (mm)	0.533	0.276
iris length l_c (mm)	4.06	7.62
iris outer loop flux occupation factor s	0.25	0.66
iris resonance frequency in presence of LGR outer loop f_{c0} (GHz)	37.2	27.4
match frequency relative to f_0, Δf(MHz)	-372	251
primary quality factor Q_P	2.8	5.6
secondary quality factor Q_S	225	245
iris reactance X_{iris} (Ω)	808	-71.1
coupling constant k_c	0.94	-0.92 j
i_c / i_o''	-1.4-2.4 j	0.57 - 0.089 j
i_{cc} / i_o''	-1.1-2.0 j	0.22 - 0.034 j
i_{Cc} / i_o''	-0.88 + 1.6 j	-1.2-0.19 j
i_i/i_o	-39-18 j	- 9.7 - 0.95 j
i_i / i_o'	-14 + 0.005 j	-15-0.005 j
i_i/i_{in}	-17 - 88 j	-25 + 85 j